JGR Space Physics

RESEARCH ARTICLE
10.1029/2022JA030983

Ionospheric Modulation by EMIC Wave-Driven Proton Precipitation: Observations and Simulations

Xingbin Tian[1,2], Yiqun Yu[1,2], Fan Gong[1,2], Longxing Ma[1,2], Jinbin Cao[1,2], Stanley C. Solomon[3], P. R. Shreedevi[4], Kazuo Shiokawa[4], Yuichi Otsuka[4], Shin-ichiro Oyama[4,5,6], and Yoshizumi Miyoshi[4]

[1]School of Space and Environment, Beihang University, Beijing, China, [2]Key Laboratory of Space Environment Monitoring and Information Processing, Ministry of Industry and Information Technology, Beijing, China, [3]National Center for Atmospheric Research, High Altitude Observatory, Boulder, CO, USA, [4]Institute for Space-Earth Environmental Research, Nagoya University, Nagoya, Japan, [5]National Institute of Polar Research, Tachikawa, Japan, [6]Space Physics and Astronomy Research Unit, University of Oulu, Oulu, Finland

Key Points:

- We report simultaneous observations of electromagnetic ion cyclotron (EMIC) waves, proton precipitation, isolated proton aurora (IPA), and ionospheric perturbation at conjugate locations
- Ionospheric density profiles in response to EMIC-associated IPA are presented for the first time
- The E region ionospheric disturbance due to EMIC-driven proton precipitation is confirmed by the Global Airglow simulation

Supporting Information:

Supporting Information may be found in the online version of this article.

Correspondence to:

Y. Yu,
yiqunyu17@gmail.com

Citation:

Tian, X., Yu, Y., Gong, F., Ma, L., Cao, J., Solomon, S. C., et al. (2023). Ionospheric modulation by EMIC wave-driven proton precipitation: Observations and simulations. *Journal of Geophysical Research: Space Physics*, *128*, e2022JA030983. https://doi.org/10.1029/2022JA030983

Received 8 SEP 2022
Accepted 9 JAN 2023

Abstract Protons of tens of keV can be resonantly scattered by electromagnetic ion cyclotron (EMIC) waves excited in the magnetosphere, resulting in proton precipitation down to the upper atmosphere. In this study, we report for the first time the ionospheric height-dependent ionization in response to EMIC-associated isolated proton aurora (IPA) using simultaneous space-borne and ground-based measurements. On 06 March 2019, the Polar Orbiting Environmental Satellites observed significant proton precipitation in the dusk sector (MLT ~ 19), while ground-based magnetometers detected a clear signature of EMIC waves. Meanwhile, the conjugated all sky imager captured an IPA and the nearby Poker Flat incoherent scatter radar (PFISR) showed enhanced electron density in the E region, suggesting a potential consequence of the EMIC wave-driven proton precipitation. The Global Airglow model simulations confirmed the dominant impact of proton precipitation on the ionosphere and agreed well with PFISR observations. This study confirmed physical links from the magnetosphere to the ionosphere through EMIC-driven proton precipitation.

Plain Language Summary Among the aurora borealis, the isolated proton aurora (IPA) is a special kind triggered by energetic protons traveling from space down to the upper atmosphere. Those protons are believed to originate from the magnetosphere where they resonantly interact with electromagnetic ion cyclotron (EMIC) waves. However, the direct observational evidence of the chain effects from the wave to ionosphere response is still lacking. This study reports for the first time simultaneous observations of the cause-and-effect relations from the long-lasting EMIC waves in space, to the incidence of a large amount of energetic protons on the top of the upper atmosphere, and lastly to the significant ionization in the ionospheric density profiles. Several in-situ and ground-based instruments were cooperatively used in this conjugate study. Numerical simulations were further employed for confirming the role of precipitating protons, rather than electrons, in causing the substantial ionization in the night-time atmosphere.

1. Introduction

Electromagnetic ion cyclotron (EMIC) waves are transverse plasma waves generated in the equatorial magnetosphere by the anisotropic energetic proton instability (Cao et al., 2005; Cornwall, 1965; Erlandson & Ukhorskiy, 2001; Morley et al., 2009; Sakaguchi et al., 2008). These EMIC waves generated in the magnetosphere can propagate along the magnetic field lines downward to the ionosphere and then be detected by the ground geomagnetic stations (Engebretson et al., 2008, 2015; Kim & Johnson, 2016; Mann et al., 2014; Perraut et al., 1984; Rauch & Roux, 1982; Wang et al., 2019; Yuan et al., 2014). During this propagation process, the EMIC waves could change their polarization near the locations of the He^+ and O^+ resonance (Johnson & Cheng, 1999; Kim & Johnson, 2016) and the left-handed polarized EMIC waves would be reflected at the Buchsbaum-resonance location (Pakhotin et al., 2022; Rauch & Roux, 1982). Although these interactions further complicate this propagation process, the EMIC waves are typically observed in the frequency range between 0.1 and 5 Hz and can be categorized into three bands according to the ion gyrofrequencies (i.e., H^+ band, He^+ band, and O^+ band). Once the wave frequency satisfies the resonance condition with the energetic protons/electrons in the magnetosphere, the particles can precipitate into the ionosphere through pitch angle scattering, which is

a significant loss process for the ring current and radiation belts (Cornwall, 1965; Hirai et al., 2018; Jordanova et al., 2001, 2007; Ni et al., 2016; Shreedevi et al., 2021; Usanova et al., 2010; Yuan et al., 2014; Zhu et al., 2022).

The particle precipitation into the Earth's atmosphere is believed to be one of the major energy sources for the ionosphere and plays an important role in modulating the dynamics of the ionospheric system (Galand et al., 2001; Hardy et al., 1989; Immel et al., 2002; Lui et al., 1977; Lyons, 1992; Miyoshi et al., 2021; Ridley et al., 2004; Thorne et al., 2010). Electron, in particular, is widely considered to be the dominant precipitating particle in the auroral zone most of the time, with the ion precipitation making a minor contribution to the total auroral energy flux, on average about 15% of electrons (Galand et al., 2001; Hardy et al., 1989). However, recent statistical and simulation results indicate that the contribution of precipitating protons cannot be neglected (Creutzberg et al., 1988; Newell et al., 2009; Tian et al., 2020; Zhu et al., 2021) and that it can lead to significant enhancements of the ionospheric conductivity in the ionospheric E region (Fang et al., 2013; Galand & Richmond, 2001; Tian et al., 2021; Yuan et al., 2014). As EMIC waves are often considered one of the major mechanisms affecting the precipitating ions in association with the isolated proton aurora (IPA) and precipitation protons likely to be the dominant source for the ionosphere (Fuselier et al., 2004; Jordanova et al., 2007; Kim et al., 2021; Nakamura et al., 2021; Ni et al., 2016; Sakaguchi et al., 2015; Tian et al., 2021), studying the influence of EMIC wave-driven precipitating protons on the ionosphere is the key to exploring the coupling process between the magnetosphere and ionosphere.

Using conjugate observations in the magnetosphere and ionosphere is an effective method to study such a coupling process. Previous studies have emphasized the importance of the EMIC wave to induce proton precipitation and subsequent effects on the ionosphere (e.g., Jordanova et al., 2007; Miyoshi et al., 2008; Tian et al., 2020; Yahnin & Yahnina, 2007). Miyoshi et al. (2008) reported precipitation of both energetic, tens of keV, protons and relativistic electrons based on ground-based and in-situ observations, and pointed out that the precipitation was caused by EMIC waves near the plasmapause. Usanova et al. (2014) also reported conjugate observations of EMIC waves and 30–800 keV proton precipitation. According to Polar Orbiting Environmental Satellites (POES) and GPS observations, Yuan et al. (2014) found that the proton precipitation caused by the EMIC waves significantly enhanced the total electron content in the ionosphere. Kim et al. (2021) reported concurrent observations of IPA driven by EMIC waves and associated local plasma disturbances in the F layer ionosphere. K. Nakamura et al. (2022); S. Nakamura et al. (2022) identified the drift electron hole caused by the pitch angle scattering with EMIC waves, and they discussed relationship to IPA. On the other hand, simulations have provided an understanding of the role of EMIC waves in modulating magnetospheric particle dynamics (Jordanova et al., 2001, 2007; Zhu et al., 2021). Recently, Tian et al. (2021) investigated the proton precipitation caused by EMIC waves and its impact on the ionosphere with a self-consistent ring current-atmosphere interactions model (RAM-SCBE) coupled with an ionospheric particle transport Global Airglow (GLOW) model. They found that proton precipitation driven by EMIC waves could not only result in a significant feedback effect on the ring current electron dynamics but also contributes largely to the ionization in the E/F regions, especially in the dusk-to-nightside sector. Based on the Monte Carlo method, Davidson (1965) and Fang et al. (2004) pointed out that although proton energy is dispersed in the F-region, the E-region is primarily impacted. Fang et al. (2013), using a coupled Monte Carlo and multistream model, presented that energetic proton precipitation are more efficient in causing secondary ionization and mainly cause ionization in E region. Although IPA has been extensively studied (e.g., Fang et al., 2013; Kim et al., 2021; Miyoshi et al., 2008), the ionosphere response is mainly represented by auroral emission and field-aligned current (FAC) or inferred by physical models. The direct observational evidences showing the chain effects of the EMIC waves on proton precipitation and subsequently on the altitude-dependent ionospheric density profiles are still lacking.

In this study, we report for the first time the ionospheric density profiles in response to EMIC-associated IPA using ground-based and space-borne observations in combination of GLOW simulations. At the magnetic conjugate locations, the intense EMIC waves, IPA, proton precipitation, and disturbances on ionospheric electron density profiles are observed by ground stations and satellite instruments. Through the usage of the GLOW model, we confirm that the observed large electron density perturbation in the E layer is mainly a result of the EMIC wave-driven proton precipitation.

2. Methodology

2.1. POES Satellites

Precipitation data of electrons and protons are obtained from the NOAA's POES. The POES satellites are Sun-synchronous low-altitude polar-orbiting spacecraft (orbit at ∼800 − 850 km and ∼102 min orbital period) and have identical instrumentation. We use particle measurements from the Medium Energy Proton and Electron Detector which measures high-energy integral electron fluxes in three energy bands (30–100 keV, 100–300 keV, and >300 keV) and proton fluxes in six energy bands (30–80 keV, 80–240 keV, 240–800 keV, 800–2,500 keV, 2,500–6,900 keV, and >6,900 keV) (Galand & Evans, 2000). The detector consists of two telescopes to detect precipitating particles (0° telescope) and geomagnetically trapped particles (90° telescope), respectively. In this paper, we use the flux data from Meteorological Operational Satellite 03 (METOP-03) with a time resolution of 2 s. We use the international geomagnetic reference field model to map the satellite position to 120 km altitude, typical altitudes of auroral emission.

2.2. Induction Magnetometer and All-Sky Imager (ASI)

Ground observations of geomagnetic pulsations are obtained from the Dawson City (DAWS, (64.05°N, 139.11°W, and $L = \sim 6.09$)) station of the Canadian Array for Realtime Investigations of Magnetic Activity (CARISMA) and the Gakona station (GAK, (62.39°N, 145.22°W, and $L = \sim 4.93$)) of the "study of dynamical variation of Particles and Waves in the Inner magnetosphere using Ground-based network observations" (PWING) project. The CARISMA is an array of magnetometer sensors designed to measure disturbances in the Earth's magnetic field (Mann et al., 2008). The PWING project uses ground-based network observations to study the dynamics of particles and waves in the inner magnetosphere (Shiokawa et al., 2017). The induction coil magnetometer data with a sampling frequency of 20 Hz (DAWS) or 64 Hz (GAK) is used to detect EMIC waves. The PWING project also operates all-sky airglow/aurora imagers, which take auroral images at several optical wavelengths. To identify the proton aurora, we use 557.7 and 486.1 nm auroral images taken at the GAK station. The electron aurora emitted by secondary electrons via proton-neutral collisions is captured by 557.7 nm auroral images, and the proton aurora emitted by the charge exchange of precipitating protons can be recorded by 486.1 nm auroral images. The time resolution of the GAK all-sky imager (ASI) is 1.5 min.

2.3. Incoherent Scatter Radar

Ionospheric electron density is obtained from the Poker Flat incoherent scatter radar (PFISR) (65.13°N, 147.47°W, and $L = \sim 5.75$). During the event (06 March 2019), PFISR was run in the four-beam mode. In this study, we selected the radar beam aligned with the local geomagnetic field (azimuth = −154.30° and elevation = 77.50°), which is the best one for estimating behaviors of field-aligned precipitating particles (Kaeppler et al., 2015). With a standard alternating code, the PFISR provides ionospheric electron density at E/F region altitudes with a height resolution of a few km (Bilitza et al., 2014; Picone et al., 2002).

2.4. Global Airglow (GLOW) Model

The GLOW model, also known as GLOW, is a toolkit of subroutines and driver programs to calculate the optical emissions in the upper atmosphere, particularly the thermosphere and ionosphere (Solomon, 2017). These emissions can result from solar-driven photon processes, auroral precipitation, and chemical reactions. The GLOW model takes precipitating electron and proton fluxes at the topside ionosphere as inputs and outputs a height distribution of ionization, electron density, and conductivity between ∼70 and ∼600 km. The model solves two-stream Boltzmann equations to model the electron moving upward or downward along magnetic field lines (Solomon, 2017). The proton transport module is computed based on the parameterization in Fang et al. (2013). They proposed a coupled Monte Carlo and multistream model to simulate the primary ionization and secondary electron ionization from energetic proton precipitation (Fang et al., 2004, 2013). The photoionization due to the solar radiation, the impact ionization from precipitating electrons and protons, and the impact ionization by the secondary electrons generated in the photoionization and ionizing collisions are considered in the model (Fang et al., 2013; Jackman et al., 1977; Solomon, 2001, 2017). The model required neutral density and temperature were taken from the empirical thermosphere model (i.e., NRLMSISE-00) (Picone et al., 2002). In this study, the

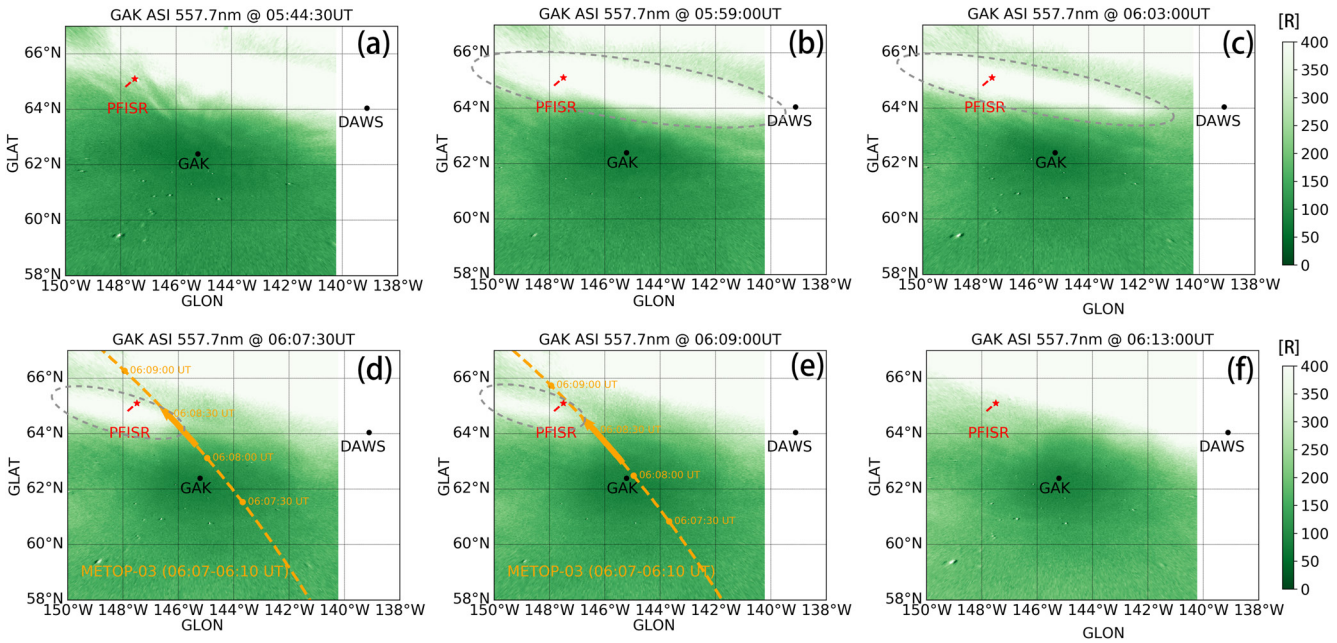

Figure 1. Auroral images of 557.7-nm taken at the Gakona station (GAK) station at different sampling periods (a–h: 05:44:30 UT to 06:13:00 UT). The images are in geographical coordinates at latitudes of 58°–67°N and longitude of 138°–150°W at an altitude of 120 km. The red star indicates the Poker Flat incoherent scatter radar and dashed line indicates its beam with azimuth = −154.30° and elevation = 77.50°. The dashed black circles indicate the isolated proton aurora region. The orange line (d and e) indicates the altitude adjusted corrected geographic footprints of Meteorological Operational Satellite 03 orbit from 06:07 to 06:10 UT and the bold line on top indicates the period with observations of significant precipitating particle flux, as shown in Figure 3. The black dots indicate the induction magnetometer stations (DAWS and GAK).

GLOW model, with an energy grid extended to ~1,000 keV, can be used to estimate the height-resolved electron density and conductivity in response to the electron and proton precipitation observed by the POES satellite.

3. Results

In this study, we report a conjugate observational event (time at ~06:00 UT, 06 March 2019) at the beginning of a substorm with a maximum auroral electrojet (AE) index of ~500 nT. Figure 1 shows 557.7-nm auroral images taken at the GAK station mapped onto an altitude of 120 km at different times with the footprints of POES trajectory and ground stations overplotted. The 486.1-nm auroral images are shown in Figure S1 in Supporting Information S1. In order to better present the IPA structure, the color scales of auroral images are optimized (Kim et al., 2021; K. Nakamura et al., 2022; S. Nakamura et al., 2022). As shown in Figure 1, from 05:43:55 UT to 06:13:00 UT, an IPA (dashed black circles) near ~66°N gradually moved westward and beyond 150°W after 06:13:00 UT. From 05:59:00 UT (Figure 1b) to 06:03:00 UT (Figure 1c), the PFISR station was right under the IPA. From 06:07 UT to 06:10 UT, the METOP-03 satellite flew over the IPA region (shown by the orange line in Figures 1d and 1e) and detected large precipitating proton fluxes as shown in Figure 3b.

The induction coil magnetometers of the GAK station and the nearby DAWS station both detected an intense EMIC wave activity from 04:30 UT to 06:30 UT. Figures 2a and 2b show the temporal evolution of the power spectrum density (PSD) of the geomagnetic pulsation (a: DAWS station, b: GAK station). Despite potential variations (e.g., the polarization reversal and Buchsbaum-resonance reflection) along the wave propagation down to the ionosphere, we assume that the observed EMIC waves on the ground could retain the wave frequency spectrum (e.g., Kim & Johnson, 2016; Mann et al., 2014; Zhu et al., 2022). In order to identify the wave bands, we use similar methods as Yuan et al. (2014). The He^+ and O^+ gyrofrequencies are calculated by the TS05 model (Tsyganenko & Sitnov, 2005) at the equatorial position where the ground stations are mapped to. From 05:10 to 06:10 UT, the PSD of the D-component geomagnetic pulsation was enhanced at the frequency of ~0.1–0.5 Hz (i.e., the band of Pc1 waves), between the O^+ gyrofrequency and He^+ gyrofrequency, suggesting a He-band EMIC wave. Such waves, excited near the equatorial plane and propagated along field lines downward (e.g., Kim & Johnson, 2016; Perraut et al., 1984; Wang et al., 2019), can trigger the precipitation of tens of keV protons and

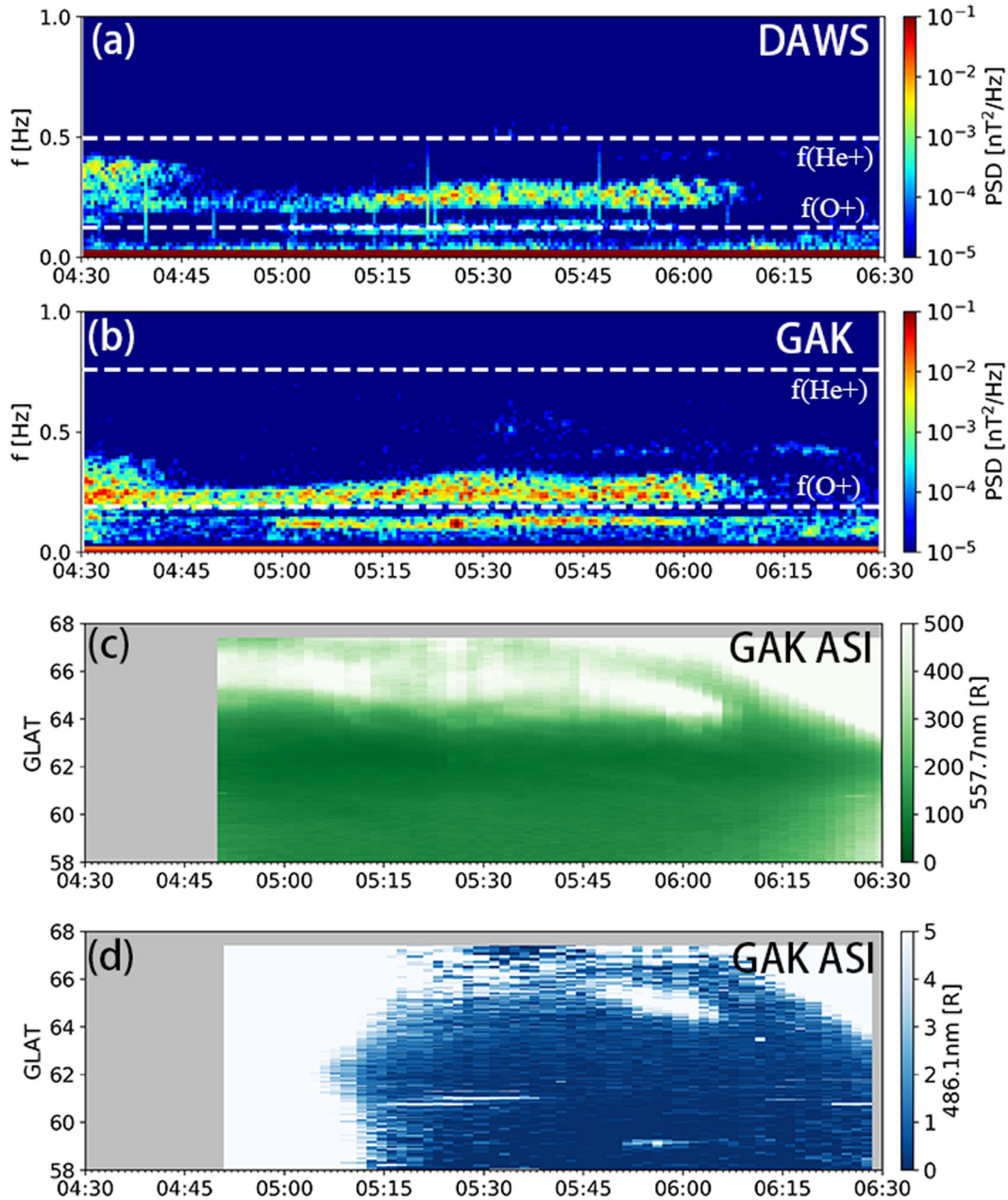

Figure 2. (a), (b) The *D*-component geomagnetic pulsation observed at the DAWS and GAK stations. (c), (d) North-south keograms of 557.7 and 486.1 nm.

ultra-relativistic electrons from the plasmasheet and radiation belt to the ionosphere (Hirai et al., 2018; Jordanova et al., 2008; Miyoshi et al., 2008; Ni et al., 2016). Those precipitating protons may be responsible for auroral emission. Figures 2c and 2d show north-south keograms of 557.7 and 486.1 nm auroral emissions mapped onto an altitude of 120 km. The auroral intensity is the average over the longitudinal range (145.12°W–145.32°W) near GAK station for each latitude. During the EMIC wave activity, 557.7 and 486.1 nm auroral emissions are detected over the latitude range of ~64°–67°. Especially around 05:45–06:09 UT, a bright IPA was observed at both 486.1 and 557.7 nm, indicating that the auroral emission was very intense at this time (see Movie S1). The appearance of the IPA showed strong correlation with the on-site EMIC wave activity, suggesting that the IPA is likely a consequence of the EMIC waves that induce proton precipitation to the upper atmosphere.

Next, we examine the linkage from the EMIC wave to the IPA, that is, particle precipitation. At about 06:08:05–06:08:30 UT, the METOP-03 satellite flew over the IPA zone and nearby ground stations. Large

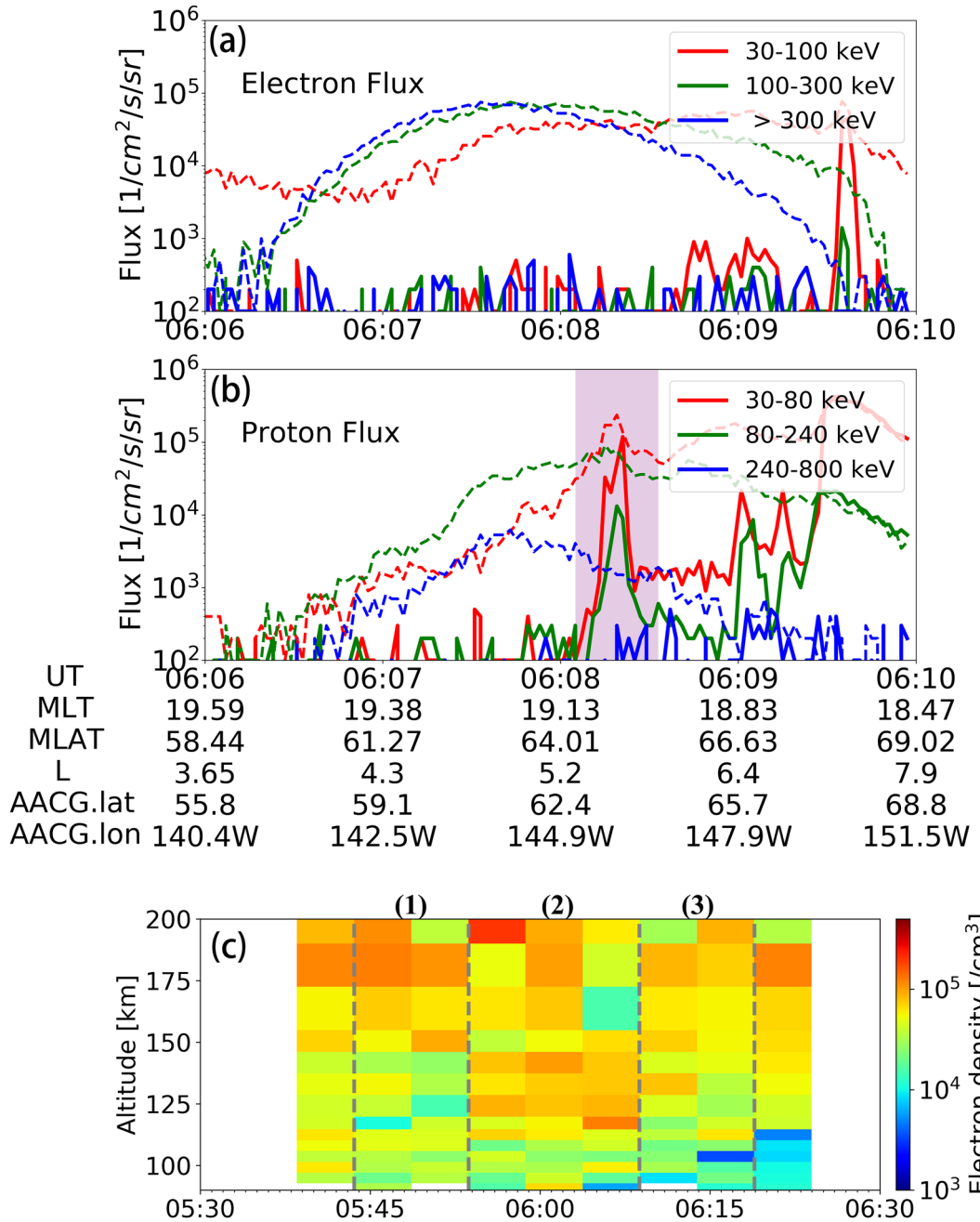

Figure 3. (a), (b) The observations of electron and proton fluxes over different energy ranges from the Meteorological Operational Satellite 03. The purple shade indicates the interval of interest when significant proton precipitation is observed. The solid and dashed color lines represent precipitating and trapping fluxes, respectively. (c) The time evolution of the height-dependent electron density from the Poker Flat incoherent scatter radar (PFISR) during 05:30 UT to 06:30 UT. The interval (1), (2), and (3) indicate the comparison time with the PFISR radar was right under or not under the isolated proton aurora region.

precipitating proton fluxes were detected within the anisotropic zone (the purple shade), as shown in Figures 3a and 3b. In the anisotropic region, precipitating fluxes (solid lines) are generally much less than trapped fluxes, but the METOP-03 satellite observed a significant enhancement of precipitating proton flux at about 06:08:21 UT for $E = 30–80$ keV, close to the level of trapped fluxes. The precipitating proton flux is much larger than electron flux. Such a substantial enhancement of precipitating proton flux is a scattering result of plasma sheet protons by EMIC waves, and a cause for the IPA.

To accurately compare the ionosphere response in the IPA region, we selected the observations where the PFISR radar was right under (05:53–06:09 UT, interval (2) in Figure 3c) or not under (05:43–05:53 UT, interval (1) and 06:09–06:19 UT, interval (3)) the IPA region for comparison. The latter two intervals represent the time when the IPA approaches and moves away from the PFISR's field of view (FOV), respectively. During these two time intervals, the PFISR was near the edge of IPA or high-latitude aurora. From about 05:53 UT to 06:09 UT, the PFISR observed considerable increase in the electron density at E region altitudes as shown in Figure 3c interval (2). The electron density was enhanced from $\sim 3 \times 10^4/\text{cm}^3$ to $\sim 10^5/\text{cm}^3$, a factor of about 3, at altitudes of 110–150 km. As the IPA moved away from the PFISR's FOV, the electron density in the E region retreated to the prior-IPA level. As no sources of photoionization were available at night time, the main energy source down to the ionosphere to cause the enhanced ionization should be carried by the EMIC wave-driven proton precipitation as described above.

Based on these observations, we can infer that the proton precipitation of tens of keV caused by the EMIC waves supplies energy source down to the ionosphere in this region. To test this hypothesis and to quantitatively understand the ionospheric response, we fit the observed precipitating flux with a Maxwellian distribution function and further use the fitted precipitating spectrum to simulate the ionospheric response using the GLOW model. During the time interval of interest in this study, the local bounce loss cone (~60°) at the POES satellites position (~800 km and magnetic latitude ~65°) is significantly larger than the telescope view (±15°), such that the detected precipitation particles by the 0° telescope are completely inside the bounce loss cone (Rodger et al., 2010, 2013; Yuan et al., 2014). We assume that the loss cone precipitating particles follow the Maxwell distribution (Codrescu et al., 1997; Yuan et al., 2014). With the measured particle flux at different energy channels, the Maxwellian functions for precipitating protons and electrons can be roughly fitted. Some fitting uncertainty is allowed as the data points used for the spectrum fitting are truly not sufficient. Since the METOP-03 satellite flew over the edge of IPA zone (as shown in Figures 1d and 1e), we use the peak flux at different energy channels to obtain the mean distribution function, and use peak flux $\times 10^{\pm 1}$ to fit the highest and lowest boundary of the spectrum. The envelope of the fitted Maxwellian functions is indicated by light pink in Figure 4a. The fitted distribution function of the precipitating proton flux is Equation 1.

$$\phi(E) = \frac{1.06 \times 10^{7\pm 1}}{2 \times 23.08^3} E exp\left(-\frac{E}{23.08}\right) \quad (1)$$

The fitted distribution of electron flux (i.e., the background) at the same region is Equation 2.

$$\phi(E) = \frac{4.98 \times 10^4}{2 \times 29.50^3} E exp\left(-\frac{E}{29.50}\right) \quad (2)$$

These precipitating spectra are input to the GLOW model to resolve the ionospheric ionization. The simulated results of electron density, Pedersen and Hall conductivity in the E/F region are shown in Figure 4b. The black-dot line represents the average value of PFISR observations from 05:53 UT to 06:09 UT (i.e., interval (2) in Figure 3c), with 25th and 75th percentiles marked by the error bars. When only the precipitating electrons are used as the model's incident energy source (green lines), the ionospheric ionization in the E region (i.e., 100–150 km) is low and deviates greatly from the observations. The minimum value of electron density (green lines) in the E region is around 5×10^3 cm^{-3}, approximately 5% of the observations. Whereas, in the F region (i.e., ~150–200 km), the simulations (green lines) are basically in agreement with the observations. This is because the major ionizing energy source in this region is background radiation, not precipitating particles. Therefore the other two simulation results in the F region (blue lines: only precipitating protons as inputs, red lines: both precipitating electrons and protons) are also in agreement with observations. When the precipitating protons are used as the only energy deposition down to the ionosphere (blue lines), the electron density is significantly enhanced in the E region. Compared to using only precipitating electrons as input, the electron density is enhanced from $\sim 5 \times 10^3$ cm^{-3} to $\sim 10^5$ cm^{-3} in the E region, while that does not change significantly in the F region. The conductivity of Pedersen and Hall show the same result, that is, E region conductivity is two orders of magnitude high as that caused by precipitating electrons and F region conductivity experiences no significant change. This is consistent with Fang et al. (2013), that tens of keV of precipitating protons can induce large ionization of the ionosphere in the E region. Specifically, precipitating protons of <10 keV mostly cause ionization enhancement above ~150 km (F region), while protons with energy >10 keV mainly induce ionization below ~150 km (E region).

When both precipitating electrons and protons are used as the energy deposition (red lines), the response of ionospheric electron density is a superposition of the above two results. The combined results of the highest boundary

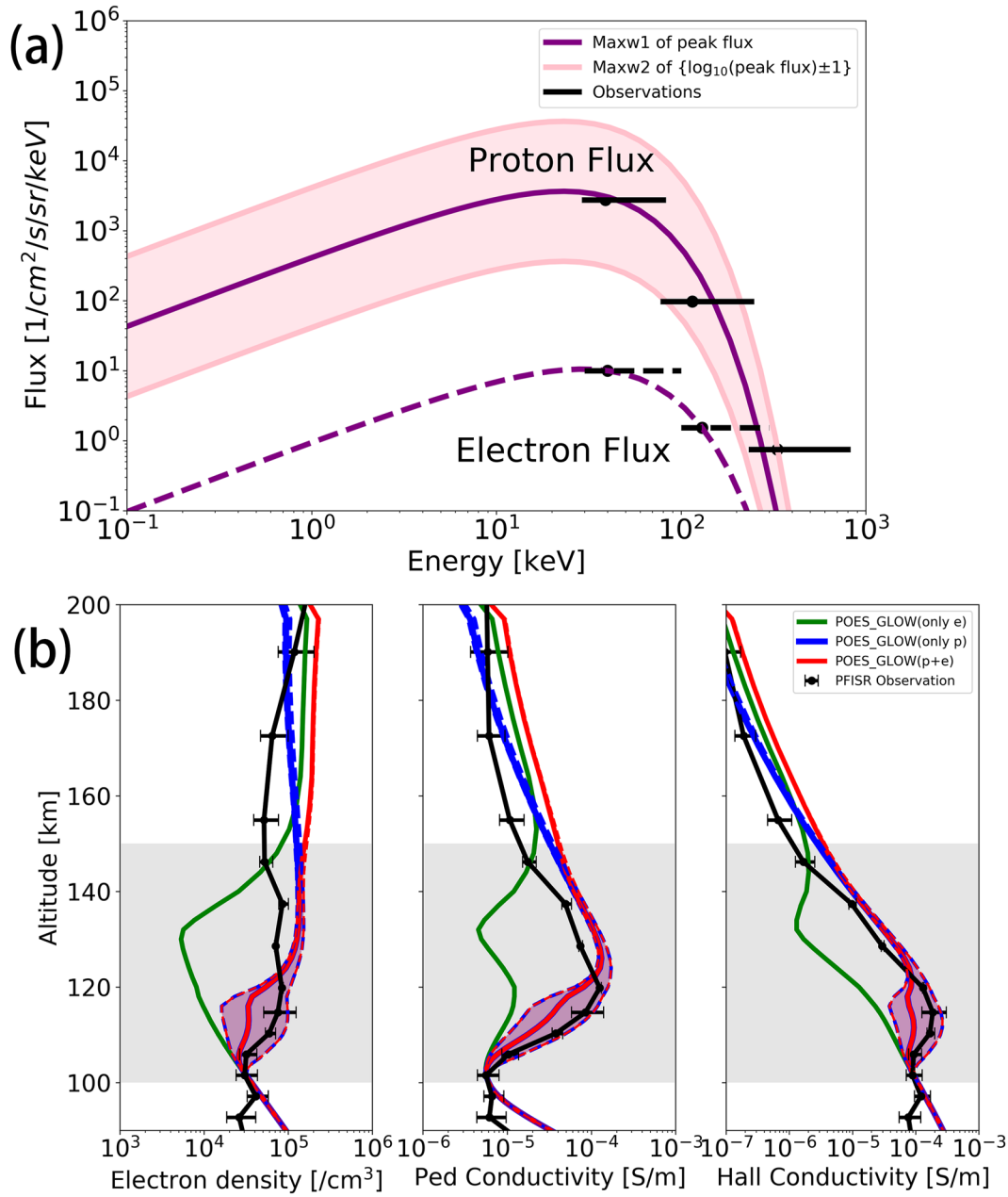

Figure 4. (a) Maxwellian energy spectra of proton and electron fluxes fitted from observations. The center of the spectrum envelope corresponds to the fitting of peak fluxes at all energy channels. The top and bottom envelop of the spectrum correspond to the fitting of the peak flux × $10^{\pm 1}$, respectively. (b) The Global Airglow model results of the height profiles of electron density, Pedersen and Hall conductivities. The colored zones hatched in reddish and bluish hues represent model results using Maxwell distributions in (a). Red areas represent results in which incident particles contain both precipitating electrons and protons; Green lines represent model results in which the incident particles are solely precipitating electrons; Blue areas indicate the model results in which the incident particles are only precipitating protons. Black dots represent the average value of Poker Flat incoherent scatter radar observations from 05:53 UT to 06:09 UT (i.e., interval (2) in Figure 3c), with 25th and 75th percentiles marked by the error bars.

of proton precipitation spectrum agree reasonably well with the observations (black dots), especially at altitudes of 100–150 km. However, the bulk model results appear to be lower than the observations in this E region. This may be caused by the slight spatiotemporal separation between the POES satellite, the PFISR and the IPA region. As the satellite flew over the edge of the IPA region, the observed precipitating flux by the POES satellite is probably smaller than that in the central zone of the IPA, under which the ionospheric response was recorded

by the PFISR. Nevertheless, from these results, it can be seen that the E region ionization and conductivity are dominantly contributed by the proton precipitation, suggesting that our hypothesis is valid. The observed EMIC wave-induced proton precipitation is indeed the main driver of the observed large ionization in the E region in this event. The electron precipitation, on the other hand, plays an insignificant role in the E region in this event. We also note that in the D region (<100 km), the ionospheric ionization appears to be enhanced in both observations and simulations. This is probably a result of geocoronal emissions of hydrogen and helium at nighttime (Solomon, 2017; Solomon & Qian, 2005).

4. Summary

Until now, the studies on the EMIC-driven IPA events have been mainly based on ground ASIs, magnetometers, and satellites (Kim et al., 2021; Yuan et al., 2014). The ionospheric response is mainly expressed in auroral emission intensity or FAC, while the understanding of ionospheric responses at different heights in the IPA zone are mostly based on physical processes or models. In this paper, we investigated the effects of magnetospheric EMIC waves on the particle precipitation, and corresponding altitudinal ionospheric response using ground- and space-based conjugate data on 06 March 2019. By using the ionospheric transport model, the contribution of precipitating electrons and protons to the ionosphere is further distinguished.

POES observations show that proton precipitation resulted from the resonant scattering by EMIC waves, is dominant over the electron precipitation and provides a primary energy deposition into the ionosphere. A strong auroral emission was observed with ASI (557.7 and 486.1 nm), underneath the POES trajectory and the PFISR radar nearby showed enhanced ionospheric electron density in the E region (∼150 km). This indicates that it could be the precipitating protons that ionize neutral particles. The results of the GLOW model based on two-stream Boltzmann equations (for electron precipitation) and parameterization (for proton precipitation) confirm that the observed precipitating protons, rather than precipitating electrons, are the reason for the largely enhanced electron density and conductivity in the E region ionosphere at altitudes above 100 km, as detected by the PFISR radar. Overall, this study provided an evidence showing comprehensive chain effects from magnetospheric waves down to upper atmosphere auroral physics and further to the height-dependent ionospheric ionization, and highlighted the important role of proton precipitation in the cross-regional coupling.

Although this event provides a good basis for conjugate observations, we are aware of some ambiguities. First, although METOP-03 satellite and PFISR detected the particle precipitation and ionospheric response (i.e., the enhanced electron density) almost at the same time, respectively, as shown in Figures 1d and 1e, both METOP-03 and PFISR were almost at the edge of IPA zone, particularly METOP-03. This led to a small spatiotemporal separation between the METOP-03 satellite and PFISR, when key IPA phenomena were observed. Second, due to insufficient energy resolutions in the precipitation flux, even with a Maxwell distribution fitting, the characteristic energy, which is the key parameter in determining the altitude of precipitation impact, still mainly depends on the lowest energy channel (i.e., 30–80 keV for protons and 30–100 keV for electrons). Thus, we used peak flux $\times 10^{\pm 1}$ to fit the highest and lowest boundary of the precipitation spectrum and the average value of PFISR observations to represent the trend of ionospheric response. Nevertheless, there was still small discrepancy between simulations and observations. This might be attributed to the small separation between those observational facilities at the time interval of interest.

Data Availability Statement

The PFISR data is accessed through the MIT Haystack Observatory Madrigal database (http://cedar.openmadrigal.org/single). The CARISMA data is available at https://www.carisma.ca/. The NOAA POES data is available at https://satdat.ngdc.noaa.gov/sem/poes/data/. The PWING ASI and induction magnetometer data are obtained via the ERG-Science Center operated by ISAS/JAXA and ISEE/Nagoya University (Miyoshi et al., 2018) (ASI data: https://ergsc.isee.nagoya-u.ac.jp/data/ergsc/ground/camera/omti/asi/, Induction magnetometer data: https://ergsc.isee.nagoya-u.ac.jp/data/ergsc/ground/geomag/isee/induction/). The GLOW model code used in the study can be obtained at http://download.hao.ucar.edu/pub/stans/glow/code/glowv0.982/. The simulation data is available at https://doi.org/10.5281/zenodo.7330793.

Acknowledgments
This work was supported by the National Natural Science Foundation of China Grants 41974192 and 41821003, and by the Fundamental Research Funds for the Central Universities. This work has been supported by JSPS KAKENHI 16H06286, 21K18651, 21H04518, 21KK0059, and 22H01283. The authors thank the CARISMA team for making available the data. CARISMA is operated by the University of Alberta, funded by the Canadian Space Agency. The authors also thank the ERG-Science Center operated by ISAS/JAXA and ISEE/ Nagoya University for the PWING ASI and induction magnetometer data.

References

Bilitza, D., Altadill, D., Zhang, Y., Mertens, C., Truhlik, V., Richards, P., et al. (2014). The international reference ionosphere 2012—A model of international collaboration. *Journal of Space Weather and Space Climate*, *4*, A07. https://doi.org/10.1051/swsc/2014004

Cao, J. B., Liu, Z. X., Yang, J. Y., Yian, C. X., Wang, Z. G., Zhang, X. H., et al. (2005). First results of low frequency electromagnetic wave detector of TC-2/double star program. *Annales Geophysicae*, *23*(8), 2803–2811. https://doi.org/10.5194/angeo-23-2803-2005

Codrescu, M. V., Fuller-Rowell, T. J., Roble, R. G., & Evans, D. S. (1997). Medium energy particle precipitation influences on the mesosphere and lower thermosphere. *Journal of Geophysical Research*, *102*(A9), 19977–19988. https://doi.org/10.1029/97JA01728

Cornwall, J. M. (1965). Cyclotron instabilities and electromagnetic emission in the ultra low frequency and very low frequency ranges. *Journal of Geophysical Research*, *70*(1), 61–69. https://doi.org/10.1029/JZ070i001p00061

Creutzberg, F., Gattinger, R., Harris, F., Wozniak, S., & Jones, A. V. (1988). Auroral studies with a chain of meridian scanning photometers, 2, Mean distributions of proton and electron aurora as a function of magnetic activity. *Journal of Geophysical Research*, *93*(A12), 14591–14601. https://doi.org/10.1029/JA093iA12p14591

Davidson, G. T. (1965). Expected spatial distribution of low-energy protons precipitated in the auroral zones. *Journal of Geophysical Research*, *70*(5), 1061–1068. https://doi.org/10.1029/jz070i005p01061

Engebretson, M., Lessard, M., Bortnik, J., Green, J., Horne, R. B., Detrick, D., et al. (2008). Pc1–Pc2 waves and energetic particle precipitation during and after magnetic storms: Superposed epoch analysis and case studies. *Journal of Geophysical Research*, *113*(A1), A01211. https://doi.org/10.1029/2007ja012362

Engebretson, M., Posch, J., Wygant, J., Kletzing, C., Lessard, M., Huang, C.-L., et al. (2015). Van Allen probes, NOAA, GOES, and ground observations of an intense emic wave event extending over 12 h in magnetic local time. *Journal of Geophysical Research: Space Physics*, *120*(7), 5465–5488. https://doi.org/10.1002/2015ja021227

Erlandson, R. E., & Ukhorskiy, A. J. (2001). Observations of electromagnetic ion cyclotron waves during geomagnetic storms: Wave occurrence and pitch angle scattering. *Journal of Geophysical Research*, *106*(A3), 3883–3895. https://doi.org/10.1029/2000ja000083

Fang, X., Liemohn, M. W., Kozyra, J. U., & Solomon, S. C. (2004). Quantification of the spreading effect of auroral proton precipitation. *Journal of Geophysical Research*, *109*(A4), A04309. https://doi.org/10.1029/2003JA010119

Fang, X., Lummerzheim, D., & Jackman, C. H. (2013). Proton impact ionization and a fast calculation method. *Journal of Geophysical Research: Space Physics*, *118*(8), 5369–5378. https://doi.org/10.1002/jgra.50484

Fuselier, S. A., Gary, S. P., Thomsen, M. F., Claflin, E. S., Hubert, B., Sandel, B. R., & Immel, T. (2004). Generation of transient dayside subauroral proton precipitation. *Journal of Geophysical Research*, *109*(A12), A12227. https://doi.org/10.1029/2004JA010393

Galand, M., & Evans, D. (2000). Radiation damage of the proton MEPED detector on POES (TIROS/NOAA) satellites.

Galand, M., Fuller-Rowell, T., & Codrescu, M. (2001). Response of the upper atmosphere to auroral protons. *Journal of Geophysical Research*, *106*(A1), 127–139. https://doi.org/10.1029/2000JA002009

Galand, M., & Richmond, A. D. (2001). Ionospheric electrical conductances produced by auroral proton precipitation. *Journal of Geophysical Research*, *106*(A1), 117–125. https://doi.org/10.1029/1999JA002001

Hardy, D. A., Gussenhoven, M., & Brautigam, D. (1989). A statistical model of auroral ion precipitation. *Journal of Geophysical Research*, *94*(A1), 370–392. https://doi.org/10.1029/JA094iA01p00370

Hirai, A., Tsuchiya, F., Obara, T., Kasaba, Y., Katoh, Y., Misawa, H., et al. (2018). Temporal and spatial correspondence of Pc1/EMIC waves and relativistic electron precipitations observed with ground-based multi-instruments on 27 March 2017. *Geophysical Research Letters*, *45*(24), 13182–13191. https://doi.org/10.1029/2018GL080126

Immel, T. J., Mende, S. B., Frey, H. U., Peticolas, L. M., Carlson, C. W., Gérard, J.-C., et al. (2002). Precipitation of auroral protons in detached arcs. *Geophysical Research Letters*, *29*(11), 1519. https://doi.org/10.1029/2001GL013847

Jackman, C. H., Garvey, R. H., & Green, A. E. S. (1977). Electron impact on atmospheric gases, I. Updated cross sections. *Journal of Geophysical Research*, *82*(32), 5081–5090. https://doi.org/10.1029/JA082i032p05081

Johnson, J. R., & Cheng, C. Z. (1999). Can ion cyclotron waves propagate to the ground? *Geophysical Research Letters*, *26*(6), 671–674. https://doi.org/10.1029/1999GL900074

Jordanova, V., Farrugia, C., Thorne, R., Khazanov, G., Reeves, G., & Thomsen, M. (2001). Modeling ring current proton precipitation by electromagnetic ion cyclotron waves during the May 14–16, 1997, storm. *Journal of Geophysical Research*, *106*(A1), 7–22. https://doi.org/10.1029/2000JA002008

Jordanova, V., Spasojevic, M., & Thomsen, M. (2007). Modeling the electromagnetic ion cyclotron wave-induced formation of detached subauroral proton arcs. *Journal of Geophysical Research*, *112*(A8), A08209. https://doi.org/10.1029/2006JA012215

Jordanova, V. K., Albert, J., & Miyoshi, Y. (2008). Relativistic electron precipitation by EMIC waves from self-consistent global simulations. *Journal of Geophysical Research*, *113*(A3), A00A10. https://doi.org/10.1029/2008JA013239

Kaeppler, S. R., Hampton, D. L., Nicolls, M. J., Strømme, A., Solomon, S. C., Hecht, J. H., & Conde, M. G. (2015). An investigation comparing ground-based techniques that quantify auroral electron flux and conductance. *Journal of Geophysical Research: Space Physics*, *120*(10), 9038–9056. https://doi.org/10.1002/2015JA021396

Kim, E.-H., & Johnson, J. R. (2016). Full-wave modeling of emic waves near the He^+ gyrofrequency. *Geophysical Research Letters*, *43*(1), 13–21. https://doi.org/10.1002/2015gl066978

Kim, H., Shiokawa, K., Park, J., Miyoshi, Y., Miyashita, Y., Stolle, C., et al. (2021). Isolated proton aurora driven by emic PC1 wave: PWING, swarm, and NOAA POES multi-instrument observations. *Geophysical Research Letters*, *48*(18), e2021GL095090. https://doi.org/10.1029/2021gl095090

Lui, A., Venkatesan, D., Anger, C., Akasofu, S.-I., Heikkila, W., Winningham, J., & Burrows, J. (1977). Simultaneous observations of particle precipitations and auroral emissions by the ISIS 2 satellite in the 19–24 MLT sector. *Journal of Geophysical Research*, *82*(16), 2210–2226. https://doi.org/10.1029/JA082i016p02210

Lyons, L. (1992). Formation of auroral arcs via magnetosphere-ionosphere coupling. *Reviews of Geophysics*, *30*(2), 93–112. https://doi.org/10.1029/92RG00002

Mann, I., Usanova, M., Murphy, K., Robertson, M., Milling, D., Kale, A., et al. (2014). Spatial localization and ducting of EMIC waves: Van Allen probes and ground-based observations (pp. 785–792). https://doi.org/10.1002/2013GL058581

Mann, I. R., Milling, D. K., Rae, I. J., Ozeke, L. G., Kale, A., Kale, Z. C., et al. (2008). The upgraded CARISMA magnetometer array in the THEMIS era. *Space Science Reviews*, *141*(1–4), 413–451. https://doi.org/10.1007/s11214-008-9457-6

Miyoshi, Y., Hori, T., Shoji, M., Teramoto, M., Chang, T. F., Segawa, T., et al. (2018). The ERG science center. *Earth Planets and Space*, *70*(1), 96. https://doi.org/10.1186/s40623-018-0867-8

Miyoshi, Y., Hosokawa, K., Kurita, S., Oyama, S. I., Ogawa, Y., Saito, S., et al. (2021). Penetration of MeV electrons into the mesosphere accompanying pulsating aurorae. *Scientific Reports*, *11*(1), 13724. https://doi.org/10.1038/s41598-021-92611-3

Miyoshi, Y., Sakaguchi, K., Shiokawa, K., Evans, D., Albert, J., Connors, M., & Jordanova, V. (2008). Precipitation of radiation belt electrons by EMIC waves, observed from ground and space. *Geophysical Research Letters*, *35*(23), L23101. https://doi.org/10.1029/2008GL035727

Morley, S. K., Ables, S. T., Sciffer, M. D., & Fraser, B. J. (2009). Multipoint observations of Pc1-2 waves in the afternoon sector. *Journal of Geophysical Research*, *114*(A9), A09205. https://doi.org/10.1029/2009JA014162

Nakamura, K., Shiokawa, K., Nosé, M., Nagatsuma, T., Sakaguchi, K., Spence, H., et al. (2022). Multi-event study of simultaneous observations of isolated proton auroras at subauroral latitudes using ground all-sky imagers and the van Allen probes. *Journal of Geophysical Research: Space Physics*, *127*(9), e2022JA030455. https://doi.org/10.1029/2022ja030455

Nakamura, K., Shiokawa, K., Otsuka, Y., Shinbori, A., Miyoshi, Y., Connors, M., et al. (2021). Simultaneous observation of two isolated proton auroras at subauroral latitudes by a highly sensitive all sky camera and Van Allen probes. *Journal of Geophysical Research: Space Physics*, *126*(5), e29078. https://doi.org/10.1029/2020JA029078

Nakamura, S., Miyoshi, Y., Shiokawa, K., Omura, Y., Mitani, T., Takashima, T., et al. (2022). Simultaneous observations of EMIC-induced drifting electron holes (EDEHs) in the Earth's radiation belt by the Arase satellite, Van Allen probes, and THEMIS. *Geophysical Research Letters*, *49*(5), e95194. https://doi.org/10.1029/2021GL095194

Newell, P., Sotirelis, T., & Wing, S. (2009). Diffuse, monoenergetic, and broadband aurora: The global precipitation budget. *Journal of Geophysical Research*, *114*(A9), A09207. https://doi.org/10.1029/2009JA014326

Ni, B., Thorne, R. M., Zhang, X., Bortnik, J., Pu, Z., Xie, L., et al. (2016). Origins of the Earth's diffuse auroral precipitation. *Space Science Reviews*, *200*(1–4), 205–259. https://doi.org/10.1007/s11214-016-0234-7

Pakhotin, I. P., Mann, I. R., Sydorenko, D., & Rankin, R. (2022). Novel EMIC wave propagation pathway through Buchsbaum resonance and inter-hemispheric wave interference: Swarm observations and modeling. *Geophysical Research Letters*, *49*(10), e98249. https://doi.org/10.1029/2022GL098249

Perraut, S., Gendrin, R., Roux, A., & de Villedary, C. (1984). Ion cyclotron waves: Direct comparison between ground-based measurements and observations in the source region. *Journal of Geophysical Research*, *89*(A1), 195–202. https://doi.org/10.1029/JA089iA01p00195

Picone, J. M., Hedin, A. E., Drob, D. P., & Aikin, A. C. (2002). NRLMSISE-00 empirical model of the atmosphere: Statistical comparisons and scientific issues. *Journal of Geophysical Research*, *107*(A12), SIA15–1–SIA15–16. https://doi.org/10.1029/2002ja009430

Rauch, J., & Roux, A. (1982). Ray tracing of ULF waves in a multicomponent magnetospheric plasma: Consequences for the generation mechanism of ion cyclotron waves. *Journal of Geophysical Research*, *87*(A10), 8191–8198. https://doi.org/10.1029/ja087ia10p08191

Ridley, A., Gombosi, T. I., & DeZeeuw, D. (2004). Ionospheric control of the magnetosphere: Conductance. In *Annales geophysicae* (Vol. 22, pp. 567–584). Copernicus GmbH. https://doi.org/10.5194/angeo-22-567-2004

Rodger, C. J., Carson, B. R., Cummer, S. A., Gamble, R. J., Clilverd, M. A., Green, J. C., et al. (2010). Contrasting the efficiency of radiation belt losses caused by ducted and nonducted whistler-mode waves from ground-based transmitters. *Journal of Geophysical Research*, *115*(A12), A12208. https://doi.org/10.1029/2010JA015880

Rodger, C. J., Kavanagh, A. J., Clilverd, M. A., & Marple, S. R. (2013). Comparison between POES energetic electron precipitation observations and riometer absorptions: Implications for determining true precipitation fluxes. *Journal of Geophysical Research: Space Physics*, *118*(12), 7810–7821. https://doi.org/10.1002/2013JA019439

Sakaguchi, K., Shiokawa, K., Miyoshi, Y., & Connors, M. (2015). Isolated proton auroras and Pc1/emic waves at subauroral latitudes. *Auroral Dynamics and Space Weather*, *215*, 59.

Sakaguchi, K., Shiokawa, K., Miyoshi, Y., Otsuka, Y., Ogawa, T., Asamura, K., & Connors, M. (2008). Simultaneous appearance of isolated auroral arcs and Pc 1 geomagnetic pulsations at subauroral latitudes. *Journal of Geophysical Research*, *113*(A5), A05201. https://doi.org/10.1029/2007JA012888

Shiokawa, K., Katoh, Y., Hamaguchi, Y., Yamamoto, Y., Adachi, T., Ozaki, M., et al. (2017). Ground-based instruments of the PWING project to investigate dynamics of the inner magnetosphere at subauroral latitudes as a part of the ERG-ground coordinated observation network. *Earth Planets and Space*, *69*(1), 160. https://doi.org/10.1186/s40623-017-0745-9

Shreedevi, P. R., Yu, Y., Ni, B., Saikin, A., & Jordanova, V. K. (2021). Simulating the ion precipitation from the inner magnetosphere by H-band and He-band electro magnetic ion cyclotron (EMIC) waves. *Journal of Geophysical Research: Space Physics*, *126*(3), e2020JA028553. https://doi.org/10.1029/2020JA028553

Solomon, S. C. (2001). Auroral particle transport using Monte Carlo and hybrid methods. *Journal of Geophysical Research*, *106*(A1), 107–116. https://doi.org/10.1029/2000JA002011

Solomon, S. C. (2017). Global modeling of thermospheric airglow in the far ultraviolet. *Journal of Geophysical Research: Space Physics*, *122*(7), 7834–7848. https://doi.org/10.1002/2017JA024314

Solomon, S. C., & Qian, L. (2005). Solar extreme-ultraviolet irradiance for general circulation models. *Journal of Geophysical Research*, *110*(A10), A10306. https://doi.org/10.1029/2005JA011160

Thorne, R. M., Ni, B., Tao, X., Horne, R. B., & Meredith, N. P. (2010). Scattering by chorus waves as the dominant cause of diffuse auroral precipitation. *Nature*, *467*(7318), 943–946. https://doi.org/10.1038/nature09467

Tian, X., Yu, Y., & Yue, C. (2020). Statistical survey of storm-time energetic particle precipitation. *Journal of Atmospheric and Solar-Terrestrial Physics*, *199*, 105204. https://doi.org/10.1016/j.jastp.2020.105204

Tian, X., Yu, Y., Zhu, M., Ma, L., Cao, J., Pr, S., et al. (2021). Effects of EMIC wave-driven proton precipitation on the ionosphere. *Journal of Geophysical Research: Space Physics*, *127*(2), e2021JA030101. https://doi.org/10.1029/2021JA030101

Tsyganenko, N. A., & Sitnov, M. I. (2005). Modeling the dynamics of the inner magnetosphere during strong geomagnetic storms. *Journal of Geophysical Research*, *110*(A3), A03208. https://doi.org/10.1029/2004JA010798

Usanova, M. E., Drozdov, A., Orlova, K., Mann, I. R., Shprits, Y., Robertson, M. T., et al. (2014). Effect of EMIC waves on relativistic and ultrarelativistic electron populations: Ground-based and Van Allen Probes observations. *Geophysical Research Letters*, *41*(5), 1375–1381. https://doi.org/10.1002/2013GL059024

Usanova, M. E., Mann, I. R., Kale, Z. C., Rae, I. J., Sydora, R. D., Sandanger, M., et al. (2010). Conjugate ground and multisatellite observations of compression-related EMIC Pc1 waves and associated proton precipitation. *Journal of Geophysical Research*, *115*(A7), A07208. https://doi.org/10.1029/2009JA014935

Wang, H., He, Y., Lühr, H., Kistler, L., Saikin, A., Lund, E., & Ma, S. (2019). Storm time EMIC waves observed by swarm and Van Allen probe satellites. *Journal of Geophysical Research: Space Physics*, *124*(1), 293–312. https://doi.org/10.1029/2018JA026299

Yahnin, A., & Yahnina, T. (2007). Energetic proton precipitation related to ion cyclotron waves. *Journal of Atmospheric and Solar-Terrestrial Physics*, *69*(14), 1690–1706. https://doi.org/10.1016/j.jastp.2007.02.010

Yuan, Z., Xiong, Y., Li, H., Huang, S., Qiao, Z., Wang, Z., et al. (2014). Influence of precipitating energetic ions caused by EMIC waves on the subauroral ionospheric E region during a geomagnetic storm. *Journal of Geophysical Research: Space Physics*, *119*(10), 8462–8471. https://doi.org/10.1002/2014JA020303

Zhu, M., Yu, Y., Cao, X., Ni, B., Tian, X., Cao, J., & Jordanova, V. K. (2022). Effects of polarization-reversed electromagnetic ion cyclotron waves on the ring current dynamics. *Earth and Planetary Physics*, *6*(4), 329–338. https://doi.org/10.26464/epp2022037

Zhu, M., Yu, Y., Tian, X., Shreedevi, P., & Jordanova, V. K. (2021). On the ion precipitation due to field line curvature (FLC) and EMIC wave scattering and their subsequent impact on the ionospheric electrodynamics. *Journal of Geophysical Research: Space Physics*, *126*, e2020JA028812. https://doi.org/10.1029/2020JA028812